

Single-step Production of Photocatalytic Surfaces via Direct Laser Interference Patterning of Titanium

Tobias Fox,^{*[a]} Pablo Maria Delfino,^[a] Francisco Cortés,^[a] Christoph Pauly,^[a] Daniel Wyn Müller,^[a] Max Briesenick,^[a] Guido Kickelbick,^[a] and Frank Mücklich^[a]

State of the art approaches to produce photocatalytic surfaces generally require multiple processing steps to achieve highly active surfaces. Following recent trends to facilitate the production of active surfaces, this work presents a single-step method to create porous photocatalytic surfaces via direct laser interference patterning (DLIP) of a titanium substrate with pulses in the picosecond range. The resulting surfaces contain a variety of titanium oxides while both their composition and morphology can be controlled through the laser process parameters. This makes it possible to tailor these surfaces for specific applications such as antimicrobial surfaces, implant

materials or water treatment. Surface characterization was executed by applying scanning electron microscopy complemented by focused ion beam cross-sectioning and energy dispersive X-ray spectroscopy as well as grazing incidence X-ray diffractometry. The photocatalytic activity achieved by different laser parameters is assessed by methylene blue degradation under UV-A light. As DLIP is already established in industrial applications, this approach could greatly facilitate the use of photocatalytic surfaces for water treatment or medical applications, as it does not require nanoparticle synthesis or additional coating steps.

Introduction

Photocatalytic materials can be used in water treatment, air purification and sterilization since they possess the ability to generate highly reactive species when irradiated with a proper light source. As a photocatalytic material, titanium dioxide shows high chemical stability, low cost and a sufficiently high bandgap energy to produce water-based radicals which makes it the most used photocatalytic material to date.^[1–5] Of the three TiO₂ allotropes that are stable at room temperature (i.e., anatase, rutile and brookite), anatase shows the highest photocatalytic activity. However, multiple studies have shown that the combination of anatase and rutile results in a significant increase in activity, as their different affinity for electrons and holes facilitates electron-hole separation and thereby prevents recombination.^[3,4,6–8] It should however be noted that a type two heterojunction between the two phases is required to enable the respective charge carriers to travel from one phase to the other. This requirement can pose a challenge especially for nanoparticle powders but also for photocatalytic surfaces with low interconnectivity of the present phases.^[9,10] The commercial product Evonik AEROXIDE® TiO₂ P25 makes use of the synergistic effects of the combination of rutile and anatase by employing 20% rutile and 80% anatase.^[11] These nanoparticles can be applied to a surface either by means of a binder

or by techniques like thermal spraying or suspension spraying. Both approaches significantly reduce the active surface of the particles and especially for the binder-based films, degradation of the binder limits the film's lifetime.^[4,12–14]

For these reasons recent research aims to facilitate the production of photocatalytic surfaces by employing single step production methods and alternative means to fixate the active agents on a carrier material. Examples for these strategies include but are not limited to: Plasma electrolytic oxidation, adsorption of nanoparticles to porous carriers, in-situ calcination of porous matrices containing active particles and the synthesis of fibrous active materials.^[5,15–18]

This work explores a bottom-up approach, where direct laser interference patterning (DLIP) is used to produce a suitable oxidic film on titanium substrates with a single processing step. Laser oxidation is a well-established process to produce dense films of titanium oxide for optical purposes or to increase corrosion resistance.^[19,20] Thereby laser based processes can have distinct advantages compared to electrolytic or chemical surface treatments as they can be incorporated in existing manufacturing chains with relative ease and can also be used for parts with complex shapes. In a recent approach relatively long pulse durations (200 ns) were used in combination with silicon monoxide particles to produce biocompatible surfaces that also showed some degree of photocatalytic activity. However, the applied laser oxidation has shown to produce mainly metastable, oxygen deficient titanium oxides which are not ideal for photocatalytic applications.^[21] Short and ultrashort pulses are more promising for the production of active surfaces as they have shown to produce oxides with high active surface areas and can produce both, anatase and rutile depending on the used fluence.^[22–27] In the experiments presented here, DLIP was applied at a pulse duration of 12 ps, since a higher amount of oxide is produced within this pulse

[a] T. Fox, P. Maria Delfino, F. Cortés, Dr. C. Pauly, D. Wyn Müller, M. Briesenick, Prof. Dr. G. Kickelbick, Prof. Dr. F. Mücklich
Chair of Functional Materials, Saarland University,
Campus D3.3, Saarbrücken 66123 (Germany)
E-mail: tobias.fox@uni-saarland.de

© 2023 The Authors. ChemNanoMat published by Wiley-VCH GmbH. This is an open access article under the terms of the Creative Commons Attribution License, which permits use, distribution and reproduction in any medium, provided the original work is properly cited.

regime than with even shorter pulses while the power density was still large enough to generate anatase.

The resulting surfaces are highly porous and contain variable stoichiometries of rutile, anatase and other metastable titanium oxides. Methylene blue (MB) degradation experiments were conducted to measure the activity of the produced surfaces, so that the influence of laser parameters like accumulated fluence and pulse number as well as the applied DLIP pattern and the cycling stability of the produced samples could be investigated.

Results and Discussion

Surface Characterization

The DLIP process used in this work not only alters the surface topography through ablation and redeposition of material but also produces a highly porous oxide layer at the topographic maxima of the pattern. To understand the effect of various laser parameters on the resulting surfaces and their photocatalytic activity a broad spectrum of varying surfaces was produced and investigated with scanning electron microscopy (SEM) and grazing incidence X-Ray diffraction (GI-XRD) before performing the methylene blue (MB) degradation assays. While the results of the MB degradation are presented for all samples, the following sections discuss the results of the surface characterization with the aid of representative images and spectra to keep the frame of this work. As explained in greater detail in the experimental section, the sample denotation follows the following scheme:

- pattern type (line/cross) and periodicity
- accumulated fluence
- number of pulses

Morphology and chemistry of the surfaces

The oxide layers produced in the DLIP process were imaged via secondary electrons and FIB cross sections. Especially the cross sections show a general trend towards deeper patterns and thicker oxide layers with increasing accumulated fluence (Figure 1). While the secondary electron (SE) contrast does not allow to distinguish between titanium substrate and the redeposited porous oxide layer, secondary ion (SI) contrast clearly separates both as the oxide shows a significantly higher sputter rate under irradiation by the Ga ion beam than the titanium substrate. This way, it could be shown that the original sample surface stayed intact at the locations with low laser power while material that was ablated at the intensity maxima of the interference pattern has agglomerated at the topographical peak regions (Figure 1f).

It is expected that oxidation occurs within the plasma plume and during material transport, similar to Zwahr et al.^[28] Hence, the valleys of the patterns act as sources for particles that can agglomerate at the topographic peaks where they are not removed by consecutive laser pulses as depicted in

Figure 2. As both nucleation and oxidation primarily occur within the plasma plume and its close vicinity the laser parameters and the existing surface are expected to affect the size of particles and agglomerates as well as their chemical composition. Since the cooling rate of matter within the plasma plume is largely a result of adiabatic cooling caused by the plumes expansion, a faster expanding plume experiences a higher cooling rate. Therefore, a lower cooling rate is expected for the deeper patterns as the plume's expansion is restricted within the patterns minima as depicted in Figure 2. Additionally, deeper patterns require a longer transportation path within the plasma plume. Both conditions are expected to increase the size and alter the phase composition of the resulting particles which is likely to affect the topography of the resulting agglomerates on the sample surface.^[29,30]

In contrast, surfaces that were produced without an interference pattern (i.e. with only a single beam) show only a thin, relatively homogenous oxide layer throughout the surface. As in this case the whole surface was exposed to laser radiation the resulting particles could not agglomerate and the oxide layer stayed thin even at high fluences as can be seen in Figure 1 h.

To verify the observations made in Figure 1 f) regarding the chemical composition, an EDS mapping was performed exemplarily on an 10-1000-3300 sample. As expected, the mapping in Figure 3 shows a clear oxygen signal in the porous structures atop the remaining titanium substrate.

Cross structures were produced by rotating the sample by 90° between two line-like patterning procedures of which each applied half the total number of pulses on the surface. The cross structures show a very similar behavior as the line pattern as an increase in accumulated fluence leads to an increase in pattern depth and oxidation. For low pulse numbers the cross shaped patterning leads to a significant removal of oxide. As can be seen in Figure 4a) the area fraction of the pattern maxima is relatively small compared to that of the minima. This leads to a relative reduction of the oxide content in the surface. In contrast, the sample depicted in Figure 4b) which was produced with high accumulated fluence shows more oxidation and almost resembles a line pattern. This is because the cross pattern is produced by two subsequent line scans and the oxide produced by the second line scan partially covers the initial pattern. A change in pulse energy between the samples 10-500-1650 (30 μJ) and 10-500-3500 (10 μJ) shows that the pulse energy affects the oxide topography as the latter, which was patterned with many low-fluence pulses shows a more porous oxide layer with a larger active surface than the sample produced with fewer, high-fluence pulses. It can however be noted that for the high fluence sample (Figure 4b) which was produced with the high pulse energy, the oxide also shows an open pored topography that rather resembles the surfaces produced with low pulse energy (Figure 4d).

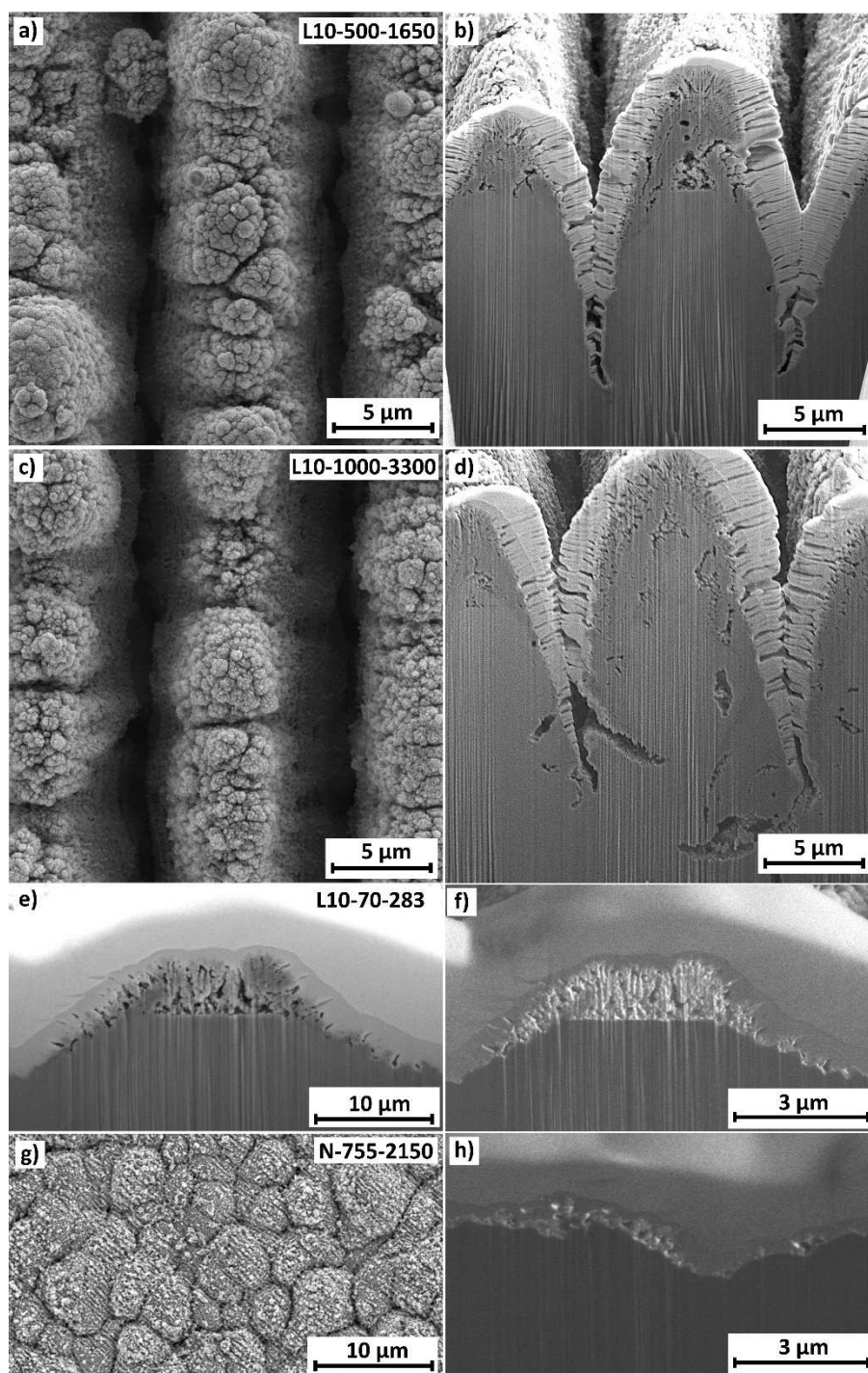


Figure 1. a–d) SEM images of surfaces with 10 μm periodicity in SE contrast and their FIB cross sections showing an increase in porosity and depth with increasing accumulated fluence. e–f) The same section of a 10 μm pattern imaged with secondary electrons (e) and secondary ions (f). The contrast created by the difference in sputter rate makes it possible to see the oxide layer in much more detail when secondary ions are used. g–h) Single-beam surface without an interference pattern (SE contrast) and cross section of its respective oxide layer (SI contrast).

Phase composition analysis

This section summarizes the most relevant findings of the performed XRD analysis with aid of representative diffractograms shown in Figure 5. As can be seen in the two diffractograms of line-like patterns L10-100-330 and L10-500-1650, a

trend towards more oxide formation for higher accumulated fluences is observed. The former, treated with 100 J/cm² shows predominantly the α-Ti peaks from the substrate as well as the metastable hongquite (TiO) phase. The second sample that was treated with 1650 pulses per point instead of 330 shows a lower Ti signal and instead, both anatase and rutile together with a

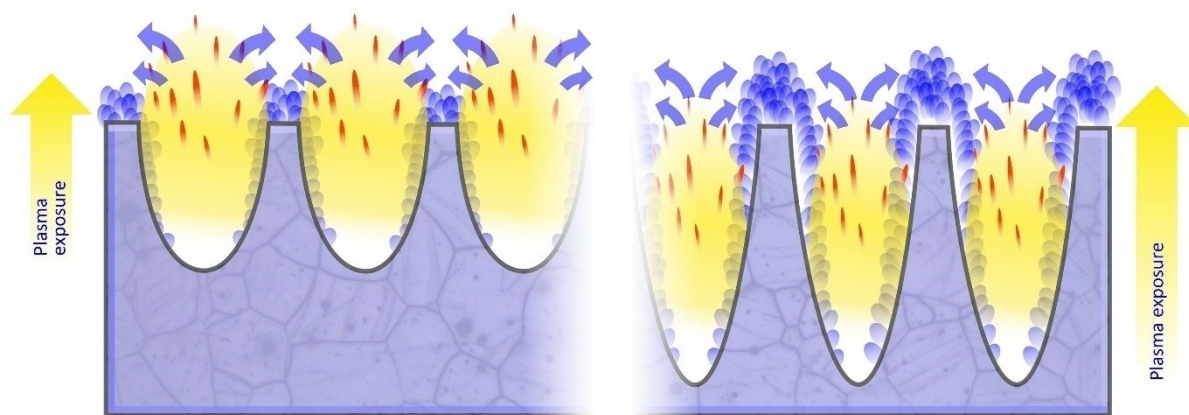


Figure 2. Proposed mechanism of material transport from topographic minima to maxima with simultaneous oxidation for shallow and deep patterns.

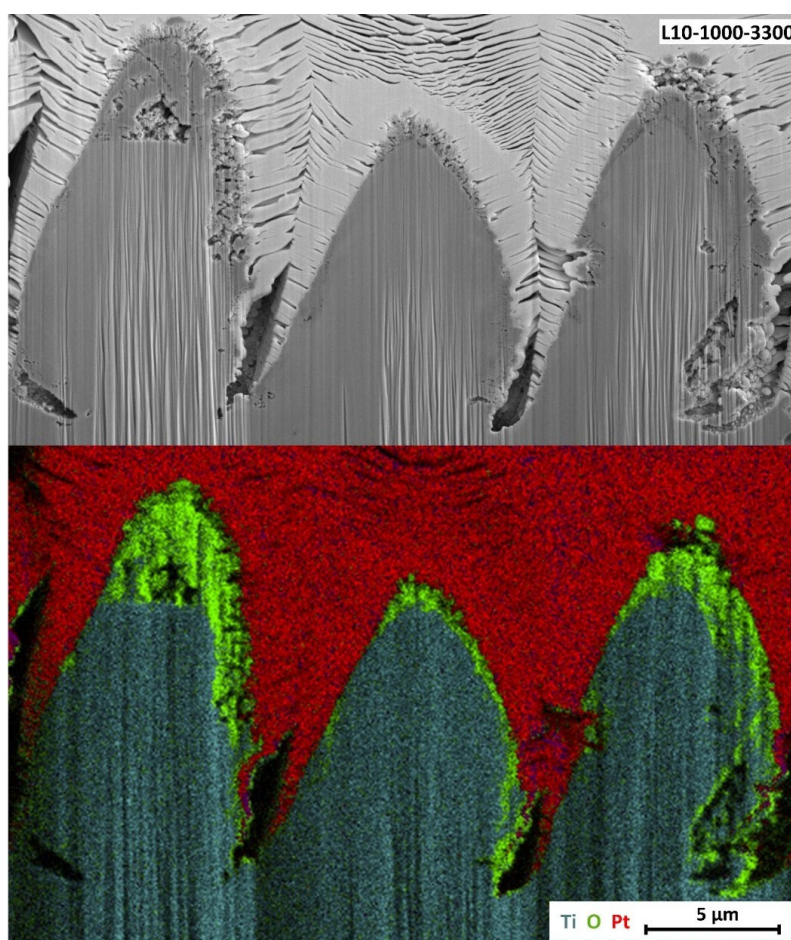


Figure 3. EDS area scan of a FIB cross section from a sample with 10 μm periodicity. The element distribution clearly shows that a porous oxide layer is present at the structure's maxima.

minor peak at 32.7° that indicates the presence of tistarite (Ti_2O_3).

The authors assume that the incomplete oxidation of the first sample is a result of the limited amount of oxygen that is present in the plasma plumes of the initial pulses. This low oxygen content not only leads to the formation of oxygen

deficient titanium oxides like TiO and Ti_2O_3 but can also cause the reduction of any existent TiO_2 by the excess titanium.^[31–33] However, if the pulse number is increased the re-ablation of these oxides leads to an increased oxygen content within the plasma which facilitates the formation of the more stable TiO_2 phases. To validate this oxidation mechanism most of the

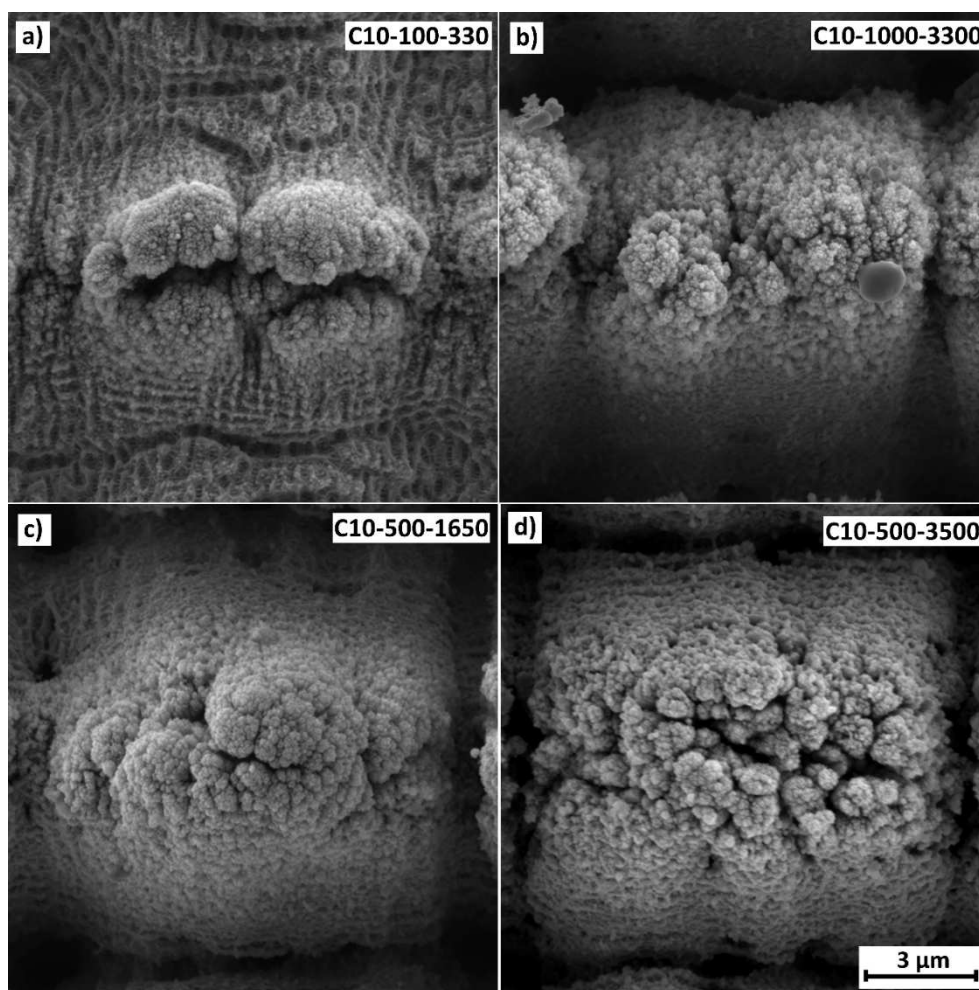


Figure 4. SEM images of cross structures. Sample C10-500-3500 was produced with the low pulse energy of 10 μ J, the rest with the high pulse energy of 30 μ J.

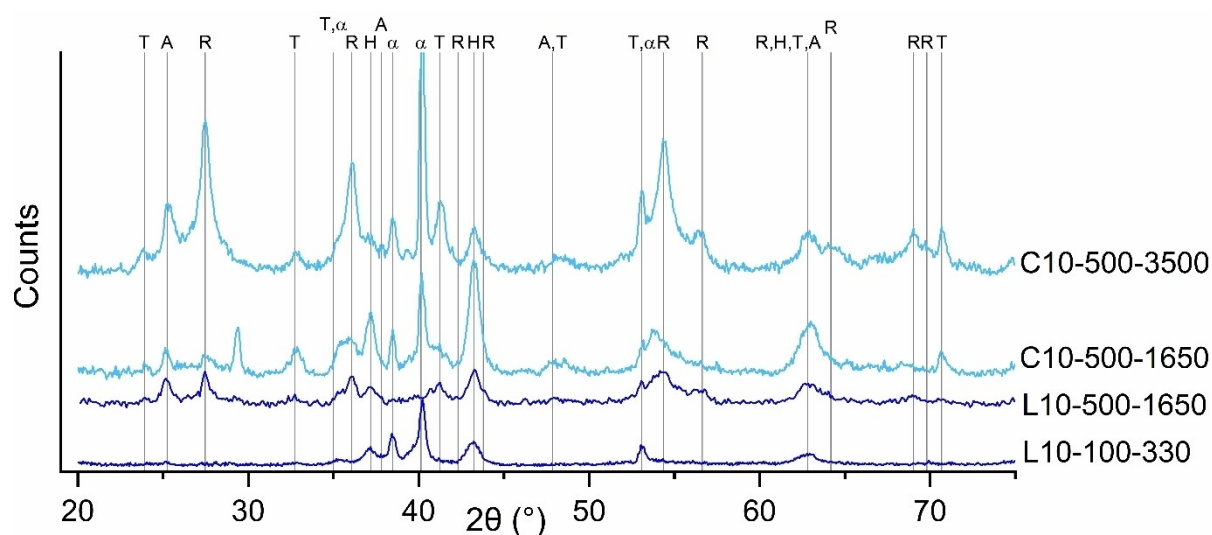


Figure 5. Diffractograms of line patterns (L) and cross patterns (C) produced with different laser parameters. The peaks are labelled as follows: α : α -Titanium; R: Rutile; A: Anatase; T: Tistarite (Ti_2O_3); H: Hongquite (TiO). The unlabelled peaks at 29.4° and 39.3° originate from the calcium carbonate in the clay that was used to fix the samples.

surface oxide was removed by ultrasonication in ethanol for 10 minutes. The resulting surface lacked the porous oxide structures and only possessed a relatively compact layer of the oxide that forms in the first stages of oxidation. Figure 6 compares the diffractogram of the ultrasonicated sample to its original state. It can be observed that the cleaning removed almost all TiO_2 and Ti_2O_3 while the intensity of the titanium substrate and the TiO phase increased. This indicates that the majority of the TiO_2 is present in the porous top layers that were deposited last while the underlying materials contains more oxygen deficient TiO.

When comparing the line pattern L10-500-1650 with the cross pattern C10-500-1650 in Figure 5, it becomes clear that although the same patterning parameters were used, the resulting surfaces present different oxide layers. The cross pattern presents more unstable oxides, namely tistarite (Ti_2O_3) and especially hongquite (TiO), and fewer rutile in its surface than the line pattern. This difference in the oxide composition likely results from the partial removal of oxide by the second scan and therefore an insufficient agglomeration of oxide in the surface. The difference in signal from the titanium substrate is probably not a result of the oxide thickness as the SEM analysis has shown that all samples possess a thick oxide layer at the structure peaks and almost none in the valleys. Instead, the difference in titanium signal likely results from the sample positioning during the XRD experiment. This is because the line pattern was aligned parallel to the incoming X-ray radiation to prevent shadowing effects. However, even a small offset in this angle could lead to a shadowing of the valleys and consequently, a lower titanium signal. As the cross-patterns are less susceptible to this misalignment and present less overall peak area they show a stronger substrate signal than the line-patterns.

When the C10-500-3500 is compared to the C10-500-1650 that was exposed to the same accumulated fluence but with a lower number of stronger pulses, it can be observed that the

latter shows a strong signal of the metastable TiO and Ti_2O_3 and less signal from anatase and rutile. As the difference in pulse energy marks the only difference between these two samples, it can be concluded that the fewer strong pulses favor the formation of the metastable TiO rather than the more stable TiO_2 phases. This effect can also be attributed to the oxide formation inside the plasma plumes produced by the individual pulses. As the stronger pulses ablate more material, the titanium to oxygen ratio favors metastable oxygen deficient oxides like TiO and Ti_2O_3 .^[31,33] In contrast, the weaker pulses ablate less material per pulse creating a more favourable titanium to oxygen ratio. Additionally, the higher number of pulses leads to a continuous re-ablation of the oxides which also increases the oxygen ratio in the plasma plume. As both, increased pressure and fast cooling rates can lead to the amorphization of particles, it is reasonable to assume that a significant portion of the observed oxide could be amorphous, which cannot be detected reliably with XRD.^[30,34] Future research should therefore focus on TEM, XPS and Kelvin probe imaging to unequivocally determine the spatial distribution of phases and the presence of heterojunctions and amorphous phase.

Methylene Blue Degradation

First parameter screening

In a first experiment, the accumulated fluence on the sample surface (F_{acc}) and the number of pulses by which this fluence was delivered (N_{acc}) were varied in a relatively low fluence regime. Additionally, two different structural periodicities (3 μm and 10 μm) were investigated. To quantify the photocatalytic activity samples were brought in contact with 50 μM methylene blue solution and exposed to UV-A light (365 nm) for 2 hours. Photocatalytic degradation of the organic methylene blue dye

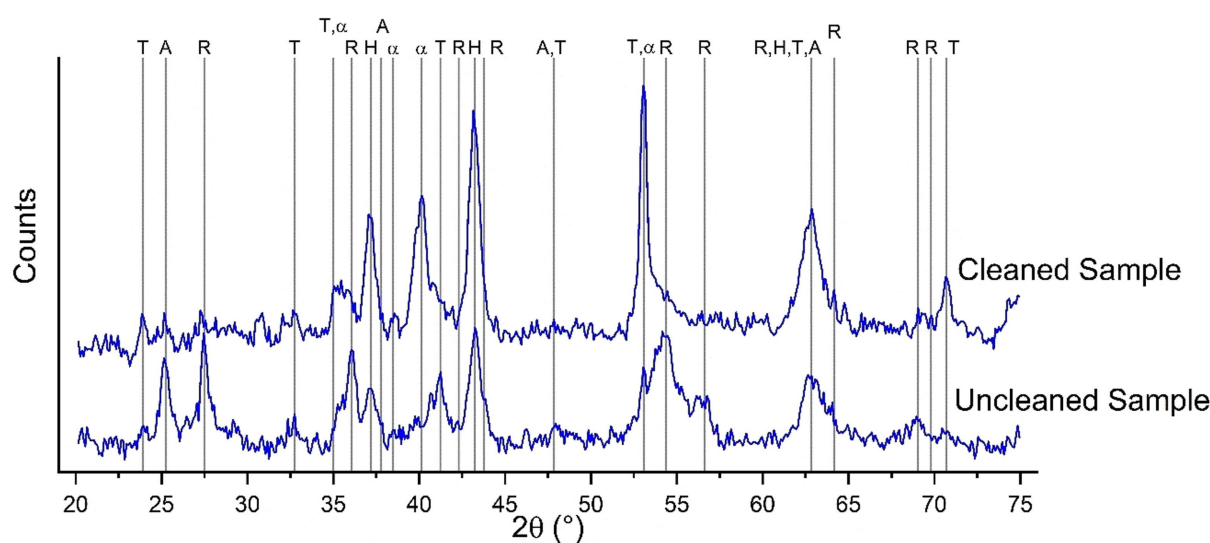


Figure 6. X-ray diffractograms of cleaned and uncleaned samples of the L10-500-1650 variant. The ultrasonic cleaning has removed most of the rutile and anatase from the surface.

causes a color change of the sample solution that can be quantified and correlated to a change in concentration using UV-Vis spectroscopy. This way the photocatalytic activity of individual samples can be compared.

The results of the methylene blue experiment are shown in Figure 7. For the plot, the concentration of the remaining solution C was normalized with the initial concentration. As expected, the titanium reference showed no activity, whereas the degradation on the other samples varies between 0% and 48%. High activity was observed especially on the samples with accumulated fluences over 700 J/cm² and over 2000 pulses per point in the surface. The pattern periodicity does not seem to play a major role. To improve the clarity of the following plots the untreated titanium references are not plotted in the subsequent figures as no significant changes could be observed.

The results depicted in Figure 7 indicate that higher accumulated fluence generally increases the photocatalytic activity. This is consistent with the observations made in the sections 2.1.1 and 2.1.2 where it was shown that higher

accumulated fluences not only produce a more porous oxide layer at the structure peaks but also tend to produce higher amounts of the photocatalytically active TiO₂ phases (especially anatase). The TiO produced by the lower accumulated fluences seems to show no relevant photocatalytic activity.

DLIP influence

To investigate the effect of the DLIP pattern on the resulting activity in more detail, surfaces without an interference pattern were produced and tested together with the line-like structures. This was done by modifying the laser setup to work with only a single beam. The laser power was adjusted accordingly, to keep the number of pulses and the accumulated fluence on the surface the same. The SEM images of the resulting surfaces in Figure 8 show that on all surfaces, a sub structure consisting of laser induced periodic surface structures (LIPSS) is observable. The periodicity of ca. 400 nm is consistent with expected values for green light on titanium.^[35,36]

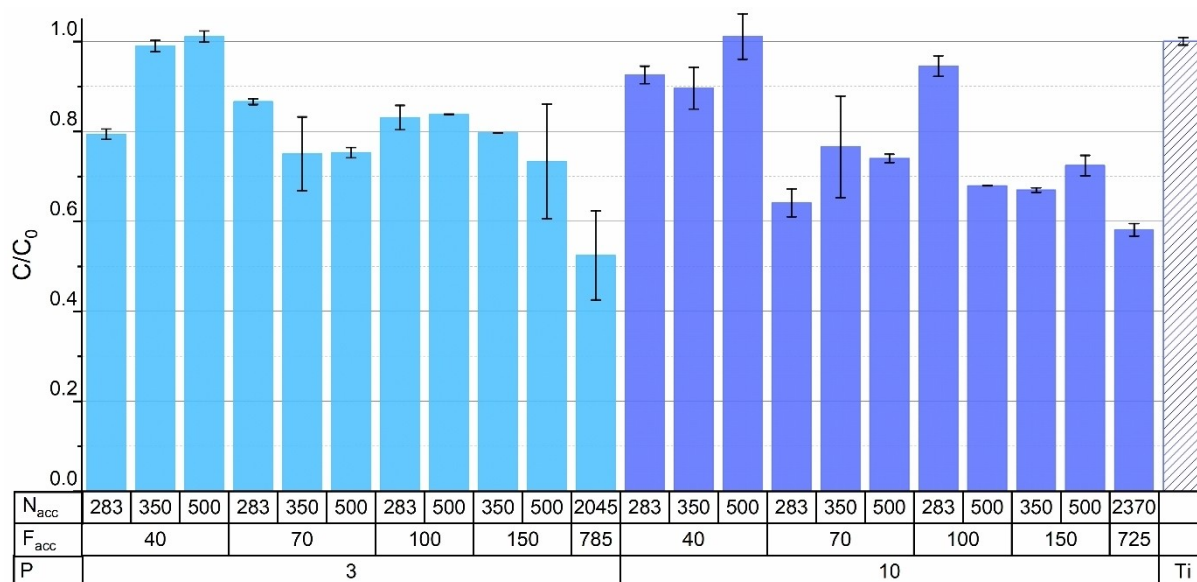


Figure 7. Change in MB-concentration achieved by different laser structures after 120 minutes of UV-A irradiation. The parameters varied are P (periodicity in μm), F_{acc} (accumulated fluence in J/cm²) and N_{acc} (number of pulses).

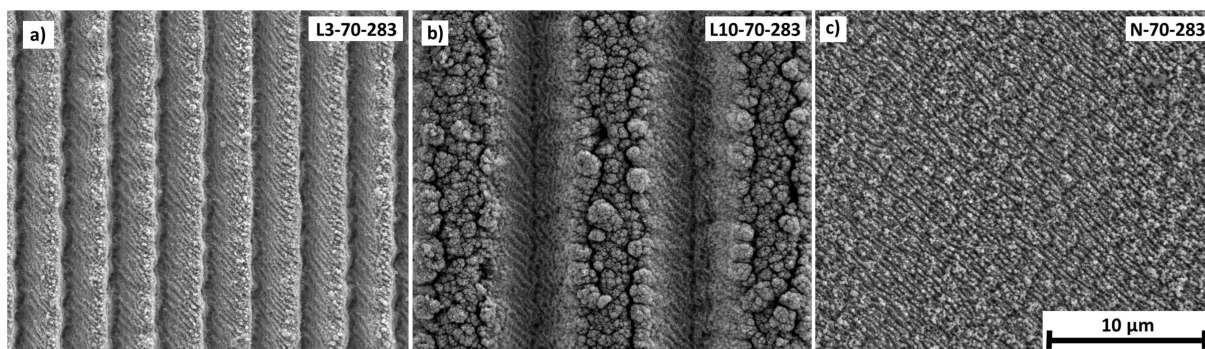


Figure 8. SEM images of samples with 3 μm periodicity, 10 μm periodicity and no interference pattern.

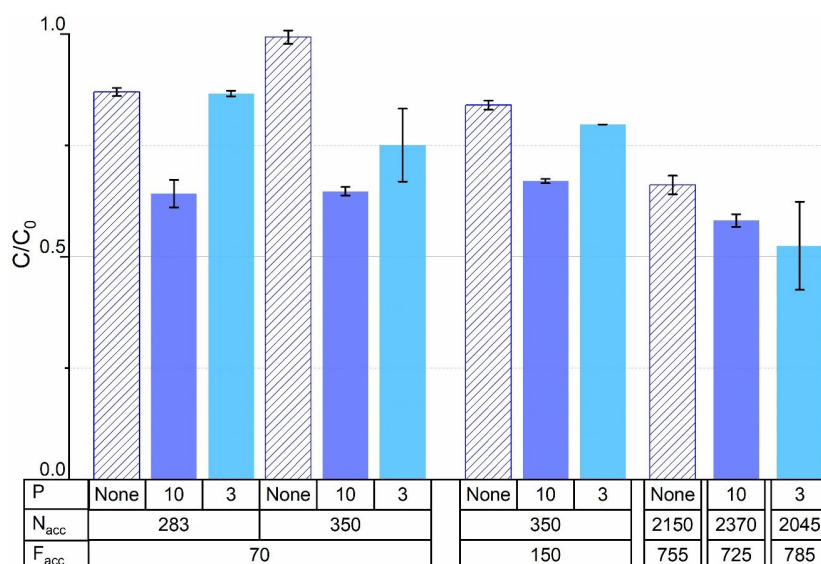


Figure 9. Effect of pattern type on MB degradation.

As can be seen from the plot in Figure 9, the two line-like patterns show a difference in reactivity for lower fluences. However, in the higher fluence regime both DLIP patterns show a larger activity than the sample that was laser-treated with only one beam.

These results can be explained by the oxide topography depicted in Figure 8. It was observed that the 10 μm interference pattern offered more space for the agglomeration of oxides while only little oxide could agglomerate on the 3 μm pattern. At higher accumulated fluences this effect was mitigated as the patterns become deeper and the topography peaks are more protected from the ablation plume occurring in the valleys. As was observed in Figure 1 the surface without interference pattern could not agglomerate oxide and instead expresses a relatively thin homogenous oxide layer that is not as photocatalytically active as the surfaces produced with a DLIP pattern.

Cycling stability

To investigate the stability of the produced surfaces over multiple cycles, two sample sets were tested four times in the same setup. All samples were cleaned with deionized water after each test to remove any residual MB. The results of the experiment are presented in Figure 10. While there is a minor trend towards a smaller activity, the overall activity did not decrease substantially over the observed number of cycles. Although promising, additional experiments are needed to ensure that the produced surfaces are stable for a number of cycles that is sufficient for industrial applications.

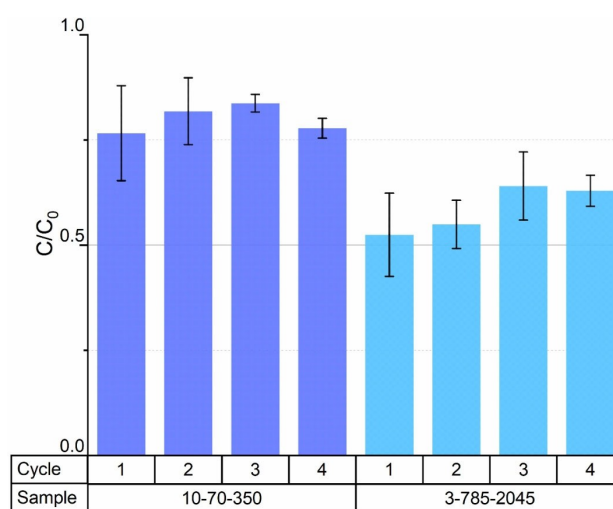


Figure 10. Cycling stability of two different surfaces over four identical cycles.

Investigation of higher accumulated fluences and cross structures

As the previous experiments showed especially promising results for higher fluences, additional experiments with accumulated fluences between 100 and 1000 J/cm^2 and both line and cross structures with 10 μm periodicity were performed.

The results presented in Figure 11 show that the general trend towards larger activities for higher accumulated fluences continues. The cross structures tend to perform better than the line-like structures especially at higher pulse numbers. Additionally, for the cross-like structures, the number of pulses plays a significant role in the resulting activity as can be seen especially in the higher fluence regime where the samples produced with relatively few stronger pulses (30 μJ per pulse) performed better

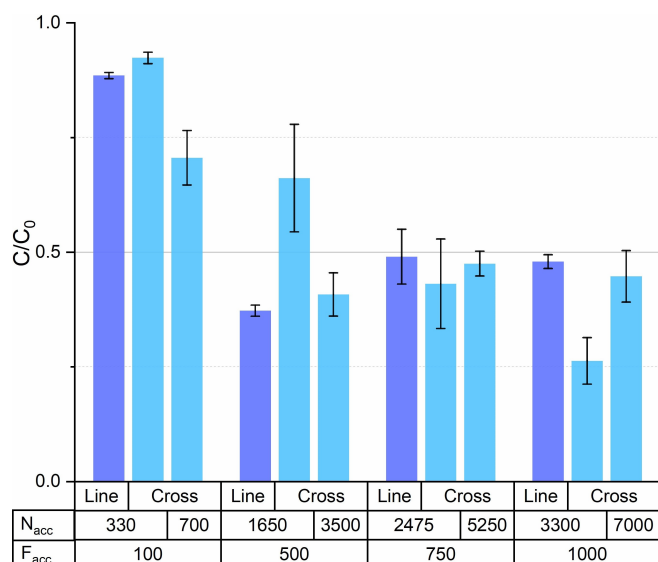


Figure 11. Cross and line structures with low and high pulse energy.

Table 1. Apparent kinetic constants after 120 minutes for the MB degradation of the line and cross patterns from Figure 11.

F _{acc} [J/cm ²]	N _{acc} [---]	k _{Cross} [1/h]	k _{Line} [1/h]
100	330	0.040 ± 0.005	0.061 ± 0.003
	700	0.175 ± 0.034	–
500	1650	0.209 ± 0.074	0.462 ± 0.045
	3500	0.449 ± 0.048	–
750	2475	0.423 ± 0.080	0.477 ± 0.124
	5250	0.372 ± 0.023	–
1000	3300	0.669 ± 0.078	0.367 ± 0.011
	7000	0.403 ± 0.051	–

than those produced with a higher number of weaker pulses (10 μJ per pulse).

When correlating the results of the methylene blue degradation with the XRD analysis it can be observed that high amounts of both rutile and anatase are found in the more active samples while the metastable oxides hongquite and tistarite seem to lower the photocatalytic activity. As previous research has shown, tistarite can increase the photocatalytic activity if heterojunctions to rutile are present. Hence, it can be assumed that the reduced activity of the C10-500-1650 sample can be attributed to the abundance of TiO as well as amorphous titanium oxides that were not be detected by the XRD.^[37,38] Additionally, as was discussed in section 2.1.1, the C10-500-1650 showed a much lower surface area than the other two samples prepared with 500 J/cm². This likely also has a negative impact on its activity. For higher accumulated fluences the effect on the surface area was less pronounced as discussed in section 2.1.1. Additionally for the higher accumulated fluences the cross structures with fewer, stronger pulses tend to express more anatase as those with many weaker pulses.

From the measurements shown in Figure 11, the respective kinetic constants *k* were calculated using Eq. (1) assuming first order degradation kinetics. Here *t* represents the duration of the experiment which was two hours. The results for are listed in Table 1.

$$k = \frac{1}{t} \ln \left(\frac{C_0}{C} \right) \quad (1)$$

As there exists a wide variety of setups to perform this kind of degradation experiments, the comparison to results of different experiments is nontrivial. Table 2 gives an overview of different setups and the degradation rates that were observed. The highest degradation rate observed in this work is highlighted. While this rate is relatively low compared to several other publications, it should be noted, that those works for the

Table 2. Overview of degradation rates of different setups. The results of this contribution are highlighted.

	Material	Kinetic constant [1/h]	Concentration of MB solution [μM]	Radiation source	Ref.
1	DLIP patterning of S-HVOF TiO ₂ sprayed coatings	0.12	10	1 μW/cm ² @ 366 nm	Toma et al. 2021 ^[12]
2	P25	0.18	100	5.3 mW/cm ² @ 360 nm	Zhang et al. 2001 ^[39]
3	P25 coated petri dish	0.25	1	Fluorescent lamp 900 mW/cm ²	Bonetta et al. 2013 ^[40]
4	Anatase/Rutile hollow nanoparticles	0.35	62.5	solar radiation	Chaudhuri et al. 2014 ^[41]
5	Nanosized TiO ₂ anatase	0.40	62.5	30 Lx	Dariani et al. 2016 ^[42]
6	DLIP Patterning of Titanium	0.67	50	Fluorescent lamp 36 W @ 365 nm	This work
7	TiO ₂ and Au–TiO ₂ composite films	0.78	11.6–16.3	60 μW/cm ² @ 365 nm	Yogi et al. 2008 ^[43]
8	Cellulose/GO/ TiO ₂ hydrogel	1.33	31	125 W Mercury lamp	Chen et al. 2020 ^[44]
9	P25	1.57	72	high pressure mercury lamp 125 W	Houas et al. 2001 ^[45]
10	TiO ₂ anatase	0.71–4.61	12.5	11–132 μW/cm ²	Wu et al. 2006 ^[46]
11	TiO ₂ nanoflowers	3	40	100 W lamp, 6.5 mW/cm ²	Harris et al. 2020 ^[47]
12	rutile anatase film	4.08	500 (Urea)	200 W Xenon-Mercury lamp	Coto et al 2021 ^[5]
13	nanosize anatase/P25	1.75–4.17	9.3	100 W longwave mercury spot lamp	Won et al. 2018 ^[48]

most part employed stronger UV-sources and worked with nanoparticle solutions instead of patterned surfaces. In practice, nanoparticles come with a set of challenges. For water treatment they need to be removed from the processed solutions to be reused and to prevent their distribution in the environment while their use on surfaces requires additional coating steps that significantly reduce the active surface of the particles.

Conclusions

In this work, photocatalytically active surfaces were created by direct laser interference patterning of a titanium substrate for the first time. The activity of the resulting surfaces was evaluated using methylene blue degradation under 365 nm UV-A radiation. The results show that the oxide layers' topography and its chemistry can be modified by adjusting the accumulated laser fluence and the number of pulses by which this fluence is brought onto the surface. An increase in accumulated fluence leads to the formation of the more stable titanium oxides – rutile and anatase –, whereas lower accumulated fluences predominantly produced the metastable oxides TiO and Ti₂O₃. A smaller pulse energy – i.e., a higher pulse number – leads to a more porous oxide layer with a larger active surface for photocatalysis. Future research should investigate the spatial distribution of the oxidic phases within the oxide layer and the presence of amorphous phases in more detail to identify processing conditions with a favourable oxide heterostructure.

Experimental Section/Methods

Sample Preparation

Wire-cut electrical discharge machining (EDM) was used to cut 5 × 5 mm samples out of a 1 mm thick titanium sheet (HMW Hanauer GmbH; 99.995 wt.%). The resulting samples were mirror-polished following a multi-step routine described in detail in a previous work.^[49]

After cleaning the samples in ethanol, the laser patterning was performed using an Edgewave px picosecond laser with a pulse width of 12 ps, a wavelength of 532 nm, a repetition rate of 100 kHz and a maximum average power of 10 W. In direct laser interference patterning a single laser beam is split into coherent sub-beams that are then brought to interference on the sample surface. The resulting interference pattern depends only on the laser's wavelength, its polarization, and the angle between the beams while the general pattern type can be adjusted by the number of beams used.^[50] Two beams are needed to create a line pattern while three or four beams can be used to produce point patterns. For the cross-like structures the samples were processed with a line pattern, rotated by 90° and processed with another line pattern.

The DLIP setup used in this work splits the main beam into four sub-beams using a diffractive optical element (DOE) as depicted in Figure 12. Behind the DOE, a prism is used to bring the beams on a parallel path before they pass the final lens and are overlapped within its focal length on the sample surface. The interference angle can be adapted by changing the distance between the prism and the DOE. At higher DEO/prism distance the beams will be more

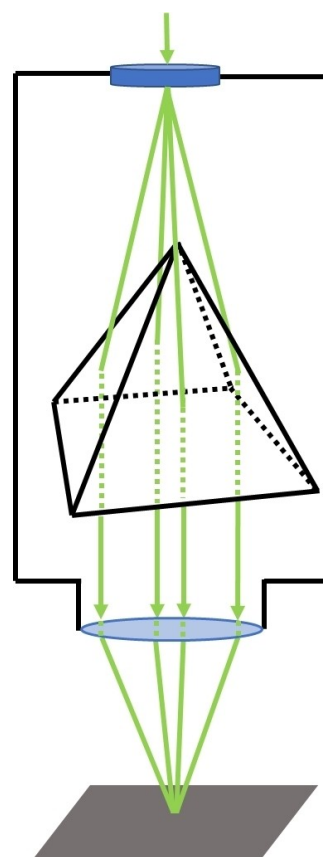


Figure 12. Simplified scheme of the DLIP optics head. The beam is first split into sub-beams, parallelized by a prism and then focused on the sample surface under an adjustable angle.

separated before being parallelized resulting in a higher interference angle and consequently a smaller DLIP periodicity P according to Eq. (2).

$$P = \frac{\lambda}{2\sin(\theta)} \quad (2)$$

The process parameters required to obtain the desired sample characteristics were calculated using a routine developed and reported in previous work.^[49] While the line patterns were produced in a single process step with two beams, for the cross patterns two perpendicular line patterns each with half the total number of pulses were overlapped. The surfaces without an interference pattern were produced by blocking all but one beam and scanning the surface with a single beam. The samples were labeled using the following scheme (Table 3).

Methylene Blue Degradation

To determine the photocatalytic activity, the samples were placed in a sample holder where each sample was exposed to 125 μ L of 50 μ M methylene blue solution. UV-irradiation was performed using a commercially available UV-source ("Nailstar" model NS-01-UK&EU) employing four fluorescent lamps with a combined power of 36 W with a centered wavelength of 365 nm in a mirrored reaction chamber. During the experiment the sample holder was covered with a UV-transparent petri dish to minimize evaporation. After an initial waiting time of 30 minutes the samples were irradiated for a

Table 3. General labelling scheme for the samples. The pattern type can be labelled C for cross patterns, L for line patterns and N for no pattern.

Parameter	Pattern type	Periodicity	Accumulated fluence	Number of pulses
Unit	–	μm	J/cm ²	–
Example	C (Cross)	10	500	1650

Table 4. ICDD PDF numbers used for the XRD phase analysis.

Phase	ICDD PDF number
α-Titanium	00-044-1294
Rutil (TiO ₂)	01-079-5858
Anatase (TiO ₂)	01-075-2545
Tistarite (Ti ₂ O ₃)	04-005-4652
Hongquiti (TiO)	04-004-2981

total of 120 min. 90 μL of solution were extracted after the experiment to determine the remaining MB concentration via UV-Vis spectroscopy. Between the experiment and the UV-Vis measurements the samples were stored for at least 24 hours. This was done in case any leuco-methylene blue that could distort the measurement formed during the experiment. The storage in ambient atmosphere ensures that any leuco-MB can oxidize back to MB so that the measurement only measures the irreversible degradation of MB.^[51] The measurements were performed with a Lambda 750 spectrometer (Perkin Elmer Inc., Shelton, USA) equipped with a 100 mm integrating sphere. To determine the MB concentrations the sample solutions were filled in disposable cuvettes with a light path of 10 mm (UV-Cuvette micro, Band GmbH, Wertheim, Germany) and diluted with 160 μL of distilled water to achieve a sufficient sample volume. A cuvette with distilled water was used as a reference to subtract the solvent absorption. Measurements were performed at a wavelength of 664 nm and an integration time of 0.2 seconds. The concentration was then determined by comparing the resulting absorption with a calibration curve. Two to three replicates were performed per parameter.

Surface Analysis

SEM/FIB/EDS

Surface imaging was conducted using the secondary electron contrast of two SEM/FIB instruments (Thermo Fisher Helios G4 PFIB CXe and FEI Helios Nanolab600). The latter was also used to perform the FIB cross sectioning using a Ga ion source. The EDS measurements were performed with the PFIB (EDAX Octane Elite Super EDS detector and APEX v2 measurement and analysis software). An accelerating voltage of 5 kV was used for both, the SEM imaging and the EDS mappings. Secondary ion imaging was done using the proprietary ICE detector in the PFIB instrument.

X-Ray diffraction

Experiments were performed using a PANalytical X'Pert Pro MPD diffractometer and Copper K_α radiation using a Goebel mirror as incident beam optics. The measurements of the cross patterns were performed in a 2Theta range of 20–75° with a step size of 0.05° and a dwell time of 35 seconds. As the line patterns presented a better signal to noise ratio, they were performed with half the counting time. To restrict the information depth to the surface layer the measurements were performed in the grazing incidence mode with

an incidence angle of 0.8°. The patterns were oriented parallel to the incident beam to minimize shadowing of the pattern valleys. The ICDD codes of the powder diffraction files (PDF) used for phase analysis are given in Table 4.

Acknowledgements

The authors gratefully acknowledge funding in the ZuMat project, supported by the State of Saarland from the European Regional Development Fund (Europäischer Fonds für regionale Entwicklung, EFRE). Funding by the German Research Foundation (DFG) for both the PFIB/SEM instrument (INST 256/510-1 FUGG) and the picosecond DLIP machine (INST 256/470-1 FUGG) is greatly acknowledged. Funding for the PFIB/SEM instrument by German Research Foundation is greatly acknowledged (INST 256/510-1 FUGG). Francisco Cortés thanks the CUA-DAHZ for the scholarship in the frame of the project I.DEAR-Materials (Project ID: D/14/07555). Pablo Delfino thanks the European Commission for the scholarship in the frame of the EMJMD AMASE (Project Nr. 619784). Open Access funding enabled and organized by Projekt DEAL.

Conflict of Interests

The authors declare no conflict of interest.

Data Availability Statement

The data that support the findings of this study are available from the corresponding author upon reasonable request.

Keywords: laser surface functionalization · direct laser interference patterning (DLIP) · photocatalytic materials · titanium oxide · methylene blue · water purification · pulsed laser ablation

- [1] S. McMichael, P. Fernández-Ibáñez, J. A. Byrne, *Water* **2021**, *13*, 1198.
- [2] H. Chouirfa, H. Bouloussa, V. Migonney, C. Falentin-Daudré, *Acta Biomater.* **2019**, *83*, 37.
- [3] J. Low, B. Cheng, J. Yu, *Appl. Surf. Sci.* **2017**, *392*, 658.
- [4] C. S. U. Demirel, C. N. Birben, M. Bekbolet, *Chemosphere* **2018**, *211*, 420.
- [5] M. Coto, S. C. Troughton, P. Knight, R. Joshi, R. Francis, R. V. Kumar, T. W. Clyne, *Surf. Coat. Technol.* **2021**, *411*, 127000.
- [6] S. G. Kumar, K. S. R. K. Rao, *Appl. Surf. Sci.* **2017**, *391*, 124.
- [7] H. M. Yadav, J. S. Kim, S. H. Pawar, *Korean J. Chem. Eng.* **2016**, *33*, 1989.
- [8] T. Kawahara, Y. Konishi, H. Tada, N. Tohge, J. Nishii, S. Ito, *Angew. Chem. Int. Ed.* **2002**, *2*, 2811.
- [9] A. Naldoni, M. Altomare, G. Zoppellaro, N. Liu, Š. Kment, R. Zbořil, P. Schmuki, *ACS Catal.* **2019**, *9*, 345.

- [10] S. Jain, R. S. Williamson, M. Marquart, A. V. Janorkar, J. A. Griggs, M. D. Roach, *J. Biomed. Mater. Res. Part B* **2018**, *106*, 2284.
- [11] A. Das, M. Patra, R. R. Wary, P. Gupta, R. G. Nair, *Conf. Ser.: Mater. Sci. Eng.* **2018**, *377*, 012101.
- [12] F. L. Toma, S. Alamri, B. Leupolt, T. Kunze, M. Barbosa, *J. Therm. Spray Technol.* **2021**, *30*, 1159.
- [13] E. Westas, M. Hayashi, F. Cecchinato, A. Wennerberg, M. Andersson, R. Jimbo, J. R. Davies, *J. Biomed. Mater. Res. Part A* **2017**, *105*, 2321.
- [14] M. A. Henderson, *Surf. Sci. Rep.* **2011**, *66*, 185.
- [15] T. Křenek, L. Vála, T. Kovářik, R. Medlín, R. Fajgar, J. Pola, V. Jandová, V. Vavruňková, M. Pola, M. Koštejn, *Dalton Trans.* **2020**, *49*, 13262.
- [16] X. Y. Sun, F. J. Zhang, C. Kong, *Colloids Surf. A* **2020**, *594*, 124653.
- [17] X. Lang, S. Gopalan, W. Fu, S. Ramakrishna, *Bull. Chem. Soc. Jpn.* **2020**, *94*, 8.
- [18] W. Wang, R. Yang, T. Li, S. Komarneni, B. Liu, *Composites Part B* **2021**, *205*, 108512.
- [19] A. J. Antończak, Ł. Skowroński, M. Trzcinski, V. V. Kinzhybalo, Ł. K. Łazarek, K. M. Abramski, *Appl. Surf. Sci.* **2015**, *325*, 217.
- [20] A. Pérez Del Pino, P. Serra, J. L. Morenza, *Appl. Surf. Sci.* **2002**, *197–198*, 887.
- [21] T. Křenek, J. Pola, D. Docheva, T. Stich, R. Fajgar, T. Kovářik, M. Pola, J. Martan, D. Moskal, V. Jandová, J. Kupčík, P. Mikysek, *Surf. Interfaces* **2021**, *26*, 101304.
- [22] O. Van Overschelde, G. Guisbiers, M. Wautelet, *J. Phys. Chem. C* **2009**, *113*, 15343.
- [23] M. Qiao, J. Yan, L. Qu, B. Zhao, J. Yin, T. Cui, L. Jiang, *ACS Appl. Mater. Interfaces* **2020**, *12*, 41250.
- [24] E. C. Landis, K. C. Phillips, E. Mazur, C. M. Friend, *J. Appl. Phys.* **2012**, *112*, 2.
- [25] T. Nakajima, T. Tsuchiya, T. Kumagai, *J. Solid State Chem.* **2009**, *182*, 2560.
- [26] H. L. Ma, J. Y. Yang, Y. Dai, Y. B. Zhang, B. Lu, G. H. Ma, *Appl. Surf. Sci.* **2007**, *253*, 7497.
- [27] C. Florian, R. Wonneberger, A. Undisz, S. V. Kirner, K. Wasmuth, D. Spaltmann, J. Krüger, J. Bonse, *Appl. Phys. A Mater. Sci. Process.* **2020**, *126*, 1.
- [28] C. Zwahr, R. Helbig, C. Werner, A. F. Lasagni, *Sci. Rep.* **2019**, *9*, 1.
- [29] E. Verrelli, D. Tsoukalas, *Solid-State Electron.* **2014**, *101*, 95.
- [30] C. G. Levi, V. Jayaram, J. J. Valencia, R. Mehrabian, *J. Mater. Res.* **1988**, *3*, 969.
- [31] B. Xu, H. Y. Sohn, Y. Mohassab, Y. Lan, *RSC Adv.* **2016**, *6*, 79706.
- [32] S. Andersson, B. Collén, U. Kuylenstierna, A. Magnéli, *Acta Chem. Scand.* **1957**, *11*, 1641.
- [33] A. S. Bolokang, D. E. Motaung, C. J. Arendse, T. F. G. Muller, *Mater. Charact.* **2015**, *100*, 41.
- [34] C. N. Huang, J. S. Bow, Y. Zheng, S. Y. Chen, N. J. Ho, P. Shen, *Nanoscale Res. Lett.* **2010**, *5*, 972.
- [35] F. Schell, S. Alamri, A. Hariharan, A. Gebert, A. F. Lasagni, T. Kunze, *Mater. Lett.* **2022**, *306*, 130920.
- [36] L. Schweitzer, A. Cunha, T. Pereira, K. Mika, A. M. B. Do Rego, A. M. Ferraria, H. Kieburg, S. Geissler, E. Uhlmann, J. Schoon, *Materials* **2020**, *13*, 5342.
- [37] M. Xu, A. Zada, R. Yan, H. Li, N. Sun, Y. Qu, *Phys. Chem. Chem. Phys.* **2020**, *22*, 4526.
- [38] S. Mergenbayeva, T. S. Atabaev, S. G. Pouloupoulos, *Catalysts* **2021**, *11*, 18.
- [39] T. Zhang, T. Oyama, A. Aoshima, H. Hidaka, J. Zhao, N. Serpone, *J. Photochem. Photobiol. A* **2001**, *140*, 163.
- [40] S. Bonetta, S. Bonetta, F. Motta, A. Strini, E. Carraro, *AMB Express* **2013**, *3*, 1.
- [41] R. Ghosh Chaudhuri, S. Paria, *Dalton Trans.* **2014**, *43*, 5526.
- [42] R. S. Dariani, A. Esmaeili, A. Mortezaali, S. Dehghanpour, *Optik* **2016**, *127*, 7143.
- [43] C. Yogi, K. Kojima, N. Wada, H. Tokumoto, T. Takai, T. Mizoguchi, H. Tamiaki, *Thin Solid Films* **2008**, *516*, 5881.
- [44] Y. Chen, Z. Xiang, D. Wang, J. Kang, H. Qi, *RSC Adv.* **2020**, *10*, 23936.
- [45] A. Houas, H. Lachheb, M. Ksibi, E. Elaloui, C. Guillard, J. M. Herrmann, *Appl. Catal., B* **2001**, *31*, 145.
- [46] C. H. Wu, J. M. Chern, *Ind. Eng. Chem. Res.* **2006**, *45*, 6450.
- [47] J. Harris, R. Silk, M. Smith, Y. Dong, W. Chen, I. N. Waterhouse, *ACS Omega* **2020**, *5*, 18919.
- [48] Y. Won, K. Schwartzberg, K. A. Gray, *Chemosphere* **2018**, *208*, 899.
- [49] T. Fox, F. Mücklich, *Adv. Eng. Mater.* **2022**, *25*, 2201021.
- [50] A. F. Lasagni, C. Gachot, K. E. Trinh, M. Hand, A. Rosenkranz, T. Roch, S. Echhardt, T. Kunze, M. Bieda, D. Günther, V. Lang, F. Mücklich, *Proc. SPIE* **2017**, *10092*, 1009211.
- [51] A. Mills, *Appl. Catal., B* **2012**, *128*, 144.

Manuscript received: July 11, 2023
 Revised manuscript received: July 13, 2023
 Accepted manuscript online: July 14, 2023
 Version of record online: August 3, 2023